Advances in Materials Research, *Vol. 14, No. 6 (2025) 511-533*
https://doi.org/10.12989/amr.2025.14.6.511

Optimization management of structures reinforced with recycled concrete aggregate mixtures incorporating ultrafine fly ash

Anber Abraheem Shlash Mohammad[1], Sultan Alaswad Alenazi[2], Badrea Al Oraini[3], Suleiman Ibrahim Mohammad[4,5], Ahmad S. Alawneh[6], Asokan Vasudevan[7,8] and Torki M. Al-Fawwaz*[9]

[1]*Digital Marketing Department, Faculty of Administrative and Financial Sciences, University of Petra, Jordan*
[2]*Marketing Department, College of Business, King Saud University, Riyadh 11362, Saudi Arabia*
[3]*Dept. Business Administration, Collage of Business and Economics, Qassim University, Qassim, Saudi Arabia*
[4]*School of Business, Al al-Bayt University, Mafraq, Jordan*
[5]*Research follower, INTI International University, 71800 Negeri Sembilan, Malaysia*
[6]*Civil Engineering Department, Al al-Bayt University, Mafraq, Jordan*
[7]*Faculty of Business and Communications, INTI International University, 71800 Negeri Sembilan, Malaysia*
[8]*Shinawatra University, 99 Moo 10, Bangtoey, Samkhok, Pathum Thani 12160 Thailand*
[9]*Department of Economics and Finance, School of Business, Al al-Bayt University, Mafraq, Jordan*

(*Received November 11, 2025, Revised November 29, 2025, Accepted December 1, 2025*)

Abstract. This paper develops a management approach to optimization of the structures that have been reinforced with recycled concrete aggregate (RCA) mixing ultrafine fly ash (UFA), and the analysis of vibration is the main concern. The analyzed structure is a plate, which rests on a Winkler-Pasternak elastic foundation, and this is done by applying higher-order shear deformation theory (HSDT), which aims at simulating the shear deformation effects in the system. To examine the vibration characteristics of the plate, a factorial design approach is employed to investigate the effects of different reinforcement ratios on structural behavior, through varying material combinations of RCA and UFA. The derivation of the governing equations of motion is done by using Hamilton's principle, which achieves a very thorough treatment of dynamic behavior, while taking into account both the material properties and the boundary conditions. For the solution of the equations, the differential quadrature method (DQM) with weighting coefficients and high-order derivatives is used, thereby guaranteeing a high level of accuracy in numerical solutions. Moreover, the Chebyshev–Gauss–Lobatto interpolation method is applied to the process of achieving the solution in order to further improve the accuracy of the solution by making the boundary conditions better approximated and by increasing the computational efficiency of the method. The experiment discloses that the dynamic response of the plate structure is greatly affected by the RCA and UFA, hence the study is able to suggest the best material combinations that would result in the least vibration amplitudes and the best structural performance. The optimization framework thereby sets up a good methodology for sustainable materials management in civil engineering applications, with the dual benefits of structures having better integrity and being environmentally friendly.

Keywords: HSDT; interpolation method; management; RCA and UFA; vibrational analysis; Winkler-Pasternak elastic foundation

*Corresponding author, Ph.D., E-mail: alfawwaz@aabu.edu.jo

http://www.techno-press.org/?journal=amr&subpage=5 ISSN: 2234-0912 (Print), 2234-179X (Online)

1. Introduction

Composite materials are a modern engineering highlight and widely used material alternatives owing to their unmatched characteristics and versatility (Abdelmalek *et al*. 2019, Al-Osta, 2022, Adeniyi *et al*. 2023). The word "composite" comes from the fact that they consist of two or more different materials combined into one new material with much better mechanical, heat, and chemical properties through an exact combination of the contributing materials (Abualnour *et al*. 2019). These materials often provide a mixture of factors, including light weight, great strength, and long life, which makes them an excellent choice for use in such demanding areas as aerospace, automotive, and civil engineering, where both performance and weight are of utmost importance (Al-Furjan *et al*. 2023). The major advantage of the composite over the traditional material has made it the first choice for engineers in their effort to construct energy-efficient, high-performance structures that consume less material and are thereby environmentally friendly (Abderezak *et al*. 2021). The composite material's ability to be engineered according to the properties needed for a specific application has completely transformed the industries and made it possible to realize optimal designs that were unattainable with the old materials before (Adeniyi *et al*. 2023). For instance, in the aviation industry, the use of composites results in a considerable reduction in the weight of the aircraft, which eventually translates into lower fuel consumption and less emission of greenhouse gases, thereby making air travel eco-friendly (Afzali *et al*. 2022). In the building industry, the application of composites in the form of structural reinforcement and rehabilitation is seen as a way of introducing corrosion resistance and long durability in such places where it is difficult for regular structures to survive over the years of a bewildering and harsh environment (Ai *et al*. 2017). Not only in structural applications but also in medical devices, sports equipment, and consumer electronics, composites are used, where high performance and reliability of the materials depend on the requirements and customized properties (Akgöz *et al*. 2018). Among these new composite materials, bio-based and nanocomposites, etc., are blossoming, and trends in sustainable engineering practices are eyeing them. For the engineers, the ever-growing composite materials are like an invitation for them to create new design solutions and to improve old ones in various disciplines (Safarpour *et al*. 2021 a). The technology and knowledge around composites are on an evolving path, hence, the role of composites in engineering will not just be pivotal but also their usage will extend to more and more applications (SafarPour *et al*. 2017). Therefore, it is becoming ever more important for engineers to acquire the know-how of composite materials and the like in order to be able to continue to render the technological advancements necessary for confronting the nowadays challenges (Ebrahimi *et al*. 2022).

New breakthroughs in material science have been a mainstay in engineering design as they basically allow the formation of heavier, lighter, and less durable materials that, together with new engineering practices, make it easier for structures and products to perform and last longer (Abderezak *et al*. 2018). The new generation of materials, like composites, nanomaterials, and bio-based substances, is capable of giving the industries, i.e., aerospace, automotive, and construction, among others, a better and greener way of working through higher efficiency, less environmental impact, and fulfilling even the strictest performance requirements (Duc *et al*. 2025). The more difficult the engineering problems become, the more the new materials developed can be tailored to meet the specific design criteria, thus optimizing both performance and cost (Garg *et al*. 2024). What is more, research into the atomic and molecular levels of material usage continues to bring up novel and environmentally friendly technology that consumes fewer resources (Zouatnia *et al*. 2019). To sum up, the continuous progress in material science gives the engineers power to go

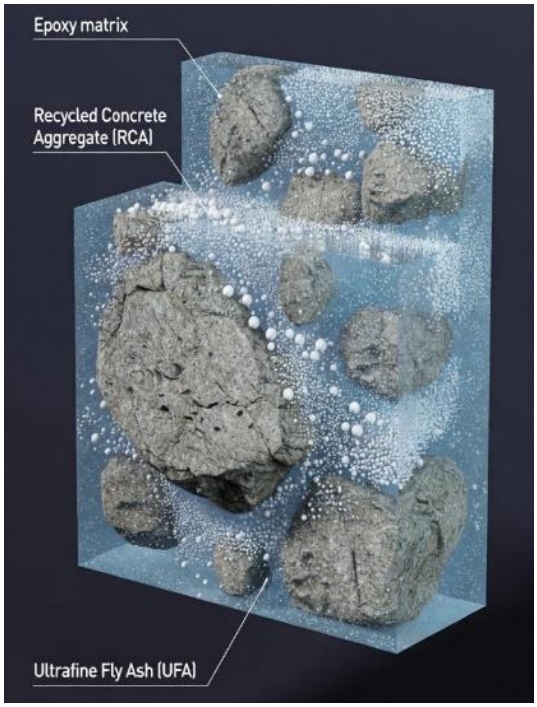

Fig. 1 A composite material designed for sustainable construction (Alhazmi *et al*. 2021, Kaleni *et al*. 2022, Nikmehr *et al*. 2022).

beyond what is possible, thus making it possible to come up with new generation designs that are suitable for addressing global problems (Jayakumari *et al*. 2024).

Stability analysis is a fundamental part of the engineer's work as it guarantees the safety and integrity of constructions and systems even under extreme loading conditions (Ahlawat *et al*. 2024). By taking into account factors like buckling, vibration, and collapse, the engineers can foresee the failure trends and eliminate the risk of the related catastrophes (Ebrahimi *et al*. 2025). Such analysis is a must in the areas of civil, mechanical, and aerospace engineering where the stability of the structure has a direct influence on performance and safety (Rahimi *et al*. 2020). Besides, stability analysis allows designers to optimize the process by revealing the most stressed areas and the need for materials, which results in more cost-effective designs (Safarpour *et al*. 2025). Ultimately, it guides the engineers in proper decision-making, thus assuring the durability and reliability of their models over a long period while at the same time saving human life and the infrastructure (Barooti *et al*. 2017). Computer simulation has become a vital component used in engineering design to the point that it is impossible to think about modern engineering without it (Selvamani *et al*. 2025). It enables engineers to create virtual representations and conduct various testing on the systems before creating the physical prototypes (Achache *et al*. 2025). The modeling and testing process has been made easier for engineers, which helps them analyze system behaviors and interactions that are complex. Real-life replication of such phenomena may be difficult, time-consuming, or expensive (Lezgy-Nazargah *et al*. 2025). By the simulations, the engineers can take care of the issues that are likely to arise at an early stage of the design process thus, lower the chances of failures happening and expensive redesigns done (Fuyad *et al*. 2024). The most various possible environmental

conditions, including with extreme factors or weird operating scenarios, can be simulated (Abdelmadjid *et al*. 2024). This helps to have a better and deeper understanding of the performance of the design and its fate in the market or usage situations at large (Sekban *et al*. 2024a). This very capability of prediction enables the designs to be optimized and thus, the production of more efficient, cheaper, and innovative products (Selvamani *et al*. 2024a). Simulation is one of the main components or aspects of the aerospace, automotive, and civil engineering industries that allows engineers to test materials, structures, and systems under various stress conditions without needing to conduct physical testing (Selvamani *et al*. 2024b). Computer simulations have also contributed to speeding up the iterative design process by allowing quick changes and improvements (Sekban *et al*. 2024b).

A composite material intended for sustainable construction applications is depicted in Fig. 1 (Alhazmi *et al*. 2021, Kaleni *et al*. 2022, Nikmehr *et al*. 2022). The microstructure features an epoxy matrix tinted blue, functioning as the main binding medium. The grey RCA particles, which are incorporated in the polymer, are considered to be the majority in recycling until landfill dumping, as their production causes less pollution than natural aggregate mining. Moreover, the presence of white, uniformly distributed UFA particles is essential. This tri-composition is a major breakthrough since it is able to synergistically improve the composite's properties. The UFA probably increases the packing density and boosts the strength of the interfacial transition zone between the RCA and the epoxy matrix, thus leading to exceptional mechanical properties as well as durability. This research represents a crucial step in the creation of high-performance, environmentally friendly construction materials, which would, in turn, make the construction industry accept the circular economy more easily.

The optimization of structures with RCA mixtures that include UFA is a very important step in the direction of sustainable construction practices. The present research mainly deals with the vibration analysis of plate structures based on the support of a Winkler-Pasternak elastic foundation, where the dynamic response is studied under different RCA and UFA material combinations. The plate is mathematically modeled via HSDT, which includes the transverse shear deformation and rotational effects, thus providing a better and more accurate representation of the structure's behavior under vibration compared to classical methods. The dynamic equations that describe the system are obtained by means of Hamilton's principle, thus setting up a proper mathematical framework that takes into account the elastic foundation and the material heterogeneity. The effects of various amounts of RCA and UFA on the structural response are studied in a factorial design manner, and the main goal is to reduce the vibration amplitudes and to optimize the material performance. The governing equations will be solved by the DQM, which makes use of high-order derivatives and weighting coefficients to ensure that the complex dynamic behavior of the system is captured accurately. In addition, the Chebyshev–Gauss–Lobatto interpolation technique is employed to boost the numerical accuracy and efficiency of the process, particularly in terms of the boundary condition approximation and the enhancement of the convergence rates. The results indicate that the use of RCA and UFA mixtures has a significant influence on the natural frequencies and vibration modes of the plate, thus opening up a possibility for the development of materials that are both eco-friendly and capable of retaining structural integrity. The optimization framework utilized in this study provides valuable insights for the design of reinforced concrete structures that are both sustainable and durable, particularly in cases where vibration control and material usage are critical considerations. The findings not only contribute to the current body of knowledge regarding the environmental sustainability of construction materials but also their impact on the performance of structures, thereby setting a stage for future research and practical applications in civil engineering.

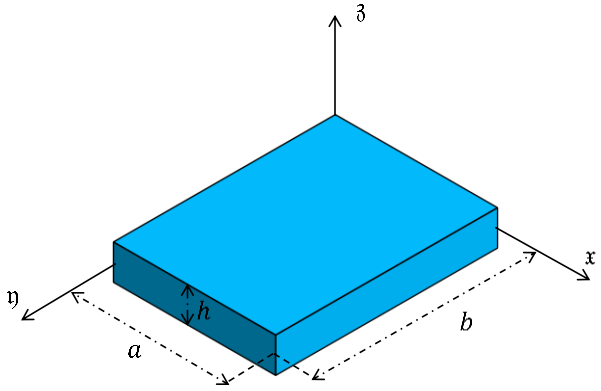

Fig. 2 The geometric parameters and coordinate system for a thick rectangular plate analyzed using the higher-order shear deformation plate theory

2. Formulation

Fig. 2 illustrates the geometric parameters and coordinate system for a thick rectangular plate analyzed using the higher-order shear deformation plate theory. This classical theory is suitable for plates where the thickness (h) is significantly smaller than the in-plane dimensions (a and b), assuming that lines normal to the mid-surface before deformation remain straight and normal to the mid-surface after deformation, and that transverse shear strain is negligible. The plate is defined within a Cartesian coordinate system, where the $x-ŋ$ plane coincides with the undeformed mid-surface, and the ʒ-axis runs through the plate's thickness. The plate is rectangular with side lengths a and b along the x and y axes, respectively. The out-of-plane deflection, is the primary unknown function of the in-plane coordinates, describing the plate's bending response to transverse loading. The plate's mechanical behavior is governed by its material properties, chiefly represented by the flexural rigidity.

The Halpin-Tsai model used for nanoclay-reinforced composites can be adapted for RCA and UFA reinforcement within an epoxy matrix. The effective Young's modulus **(E_c)** of the composite can be estimated as follows:

$$E_c = E_m \times ((1 + 2\eta W_{RCA+UFA}) / (1 - \eta W_{RCA+UFA})) \quad (1)$$

where E_c, E_m, $W_{RCA+UFA}$, and η show the effective Young's modulus of the composite, Young's modulus of the matrix material, volume fraction of the combined RCA and UFA (mixture) reinforcement in the composite, and reinforcement efficiency parameter, which accounts for the reinforcement's shape, distribution, and orientation, respectively. The reinforcement efficiency parameter (η) is defined similarly to the nanoclay model, but here it will depend on the Young's modulus of RCA (E_1) and UFA (E_2):

$$\eta = \left((E_f/E_m) - 1\right)/\left((E_f/E_m) - 2\zeta\right) \quad (2)$$

where E_f is the effective Young's modulus of the RCA and UFA mixture. ζ is a parameter related to the shape and orientation of the reinforcement (RCA and UFA). For a uniform distribution, the effective Young's modulus (E_f) of the RCA-UFA mixture can be approximated as:

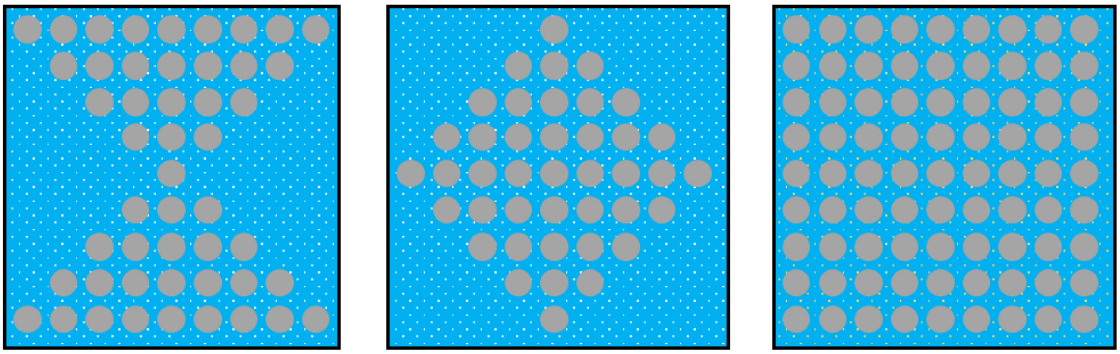

a) Pattern X *b) Pattern O* *c) Pattern UD*

Fig. 3 Various distribution patterns of presented composite reinforcement

$$E_f = x_1.E_{RCA} + x_2.E_{UFA} \tag{3}$$

where E_{RCA} and E_{UFA} are the individual Young's moduli of RCA and UFA, respectively. In This equation, x_1 and x_2 are the volume fractions of RCA and UFA in the mixture. The Poisson's ratio (ϑ_c) of the composite is calculated using a weighted average of the Poisson's ratios of the individual components (epoxy, RCA, and UFA):

$$\vartheta_c = \vartheta_m \times (1 - W_{RCA+UFA}) + \vartheta_f \times W_{RCA+UFA} \tag{4}$$

where ϑ_c, ϑ_m, and ϑ_f present the Poisson's ratio of the composite, Poisson's ratio of the matrix, and Poisson's ratio of the RCA and UFA, respectively. For the reinforcement mixture:

$$\vartheta_f = x_1.\vartheta_{RCA} + x_2.\vartheta_{UFA} \tag{4}$$

where ϑ_{RCA} and ϑ_{UFA} are the Poisson's ratios of RCA and UFA, respectively. The density of the composite is given by the rule of mixtures for density:

$$\rho_c = \rho_m \times (1 - W_{RCA+UFA}) + \rho_f \times W_{RCA+UFA}, \tag{6}$$

where ρ_c, ρ_m, and ρ_f present the density of the composite, the density of the matrix, and the density of the RCA-UFA mixture, respectively. For the reinforcement mixture:

$$\rho_f = x_1.\rho_{RCA} + x_2.\rho_{UFA} \tag{7}$$

where ρ_{RCA} and ρ_{UFA} are the densities of RCA and UFA, respectively. The distribution of RCA and UFA in the epoxy matrix can significantly affect the composite properties. The volume fraction of the reinforcement, $W_{RCA+UFA}$, is defined as the ratio of the total volume of RCA and UFA to the total volume of the composite material. Various distribution patterns (denoted as Pattern O, Pattern UD, and Pattern X) are used to model different arrangements of the reinforcement within the matrix.

Pattern O: $V_{RCA+UFA}(\mathfrak{z}) = 2(1 - \frac{|\mathfrak{z}|}{h})V^*_{RCA+UFA}$, (8a)

Pattern UD: $V_{RCA+UFA}(\mathfrak{z}) = V^*_{RCA+UFA}$, (8b)

$$\text{Pattern X: } V_{RCA+UFA}(\mathfrak{z}) = 4\frac{|\mathfrak{z}|}{h}V^*_{RCA+UFA}, \tag{8c}$$

where the total volume percentage of nanocomposite is denoted by $V^*_{RCA+UFA}$. It remains steady and unaffected by the distributions of nanocomposite. It may be expressed like this:

$$V^*_{RCA+UFA} = \frac{W_{RCA+UFA}}{W_{RCA+UFA} + \rho_c/\rho_m - W_{RCA+UFA} \times \frac{\rho_c}{\rho_m}} \tag{9}$$

Various distribution patterns of presented composite reinforcement (Recycled concrete aggregate mixtures incorporating ultrafine Fly ash) are shown in Fig. 3. In this figure, the blue matrix is made of epoxy resin, while the gray stones represent recycled concrete aggregates, and the small white dots are ultrafine fly ash.

3. Governing equations

3.1 Displacement fields

The displacement fields are provided as follows when HSDT is used to represent them (Jha *et al*. 2012):

$$\begin{gathered}
\mathfrak{u}(\mathfrak{x},\mathfrak{y},\mathfrak{z},\mathfrak{t}) = \mathfrak{u}_0(\mathfrak{x},\mathfrak{y},\mathfrak{t}) + \mathfrak{z}\mathfrak{u}_1(\mathfrak{x},\mathfrak{y},\mathfrak{t}) + \mathfrak{z}^2\mathfrak{u}_2(\mathfrak{x},\mathfrak{y},\mathfrak{t}) + \mathfrak{z}^3\mathfrak{u}_3(\mathfrak{x},\mathfrak{y},\mathfrak{t}),\\
\mathfrak{v}(\mathfrak{x},\mathfrak{y},\mathfrak{z},\mathfrak{t}) = \mathfrak{v}_0(\mathfrak{x},\mathfrak{y},\mathfrak{t}) + \mathfrak{z}\mathfrak{v}_1(\mathfrak{x},\mathfrak{y},\mathfrak{t}) + \mathfrak{z}^2\mathfrak{v}_2(\mathfrak{x},\mathfrak{y},\mathfrak{t}) + \mathfrak{z}^3\mathfrak{v}_3(\mathfrak{x},\mathfrak{y},\mathfrak{t}),\\
\mathfrak{w}(\mathfrak{x},\mathfrak{y},\mathfrak{z},\mathfrak{t}) = \mathfrak{w}_0(\mathfrak{x},\mathfrak{y},\mathfrak{t}) + \mathfrak{z}\mathfrak{w}_1(\mathfrak{x},\mathfrak{y},\mathfrak{t}) + \mathfrak{z}^2\mathfrak{w}_2(\mathfrak{x},\mathfrak{y},\mathfrak{t}) + \mathfrak{z}^3\mathfrak{w}_3(\mathfrak{x},\mathfrak{y},\mathfrak{t}).
\end{gathered} \tag{10}$$

where $(\mathfrak{u},\mathfrak{v},\mathfrak{w})$ are the axial displacement components of an arbitrary point $(\mathfrak{x},\mathfrak{y},\mathfrak{z})$ within the domain, $(\mathfrak{u}_0,\mathfrak{v}_0,\mathfrak{w}_0)$ are the corresponding components at the reference mid-plane, $(\mathfrak{u}_1,\mathfrak{v}_1,\mathfrak{w}_1)$ are the normal rotations about the $\mathfrak{y}$-, $\mathfrak{x}$-, and $\mathfrak{z}$-axis, respectively, and $\mathfrak{u}_2$, $\mathfrak{v}_2$, $\mathfrak{w}_2$, $\mathfrak{u}_3$, $\mathfrak{v}_3$ and $\mathfrak{w}_3$ present the higher-order terms in the Taylor's series expansion. Furthermore, the core layer's stress-strain relationships may be expressed as follows (Reddy, 2003):

$$\begin{gathered}
\sigma_{\mathfrak{x}\mathfrak{x}} = \mathfrak{q}_{11}\varepsilon_{\mathfrak{x}\mathfrak{x}} + \mathfrak{q}_{12}\varepsilon_{\mathfrak{y}\mathfrak{y}} + \mathfrak{q}_{13}\varepsilon_{\mathfrak{z}\mathfrak{z}},\\
\sigma_{\mathfrak{y}\mathfrak{y}} = \mathfrak{q}_{21}\varepsilon_{\mathfrak{x}\mathfrak{x}} + \mathfrak{q}_{22}\varepsilon_{\mathfrak{y}\mathfrak{y}} + \mathfrak{q}_{23}\varepsilon_{\mathfrak{z}\mathfrak{z}},\\
\sigma_{\mathfrak{z}\mathfrak{z}} = \mathfrak{q}_{13}\varepsilon_{\mathfrak{x}\mathfrak{x}} + \mathfrak{q}_{23}\varepsilon_{\mathfrak{y}\mathfrak{y}} + \mathfrak{q}_{33}\varepsilon_{\mathfrak{z}\mathfrak{z}},\\
\tau_{\mathfrak{y}\mathfrak{z}} = \mathfrak{q}_{44}\gamma_{\mathfrak{y}\mathfrak{z}},\\
\tau_{\mathfrak{x}\mathfrak{z}} = \mathfrak{q}_{55}\gamma_{\mathfrak{x}\mathfrak{z}},\\
\tau_{\mathfrak{x}\mathfrak{y}} = \mathfrak{q}_{66}\gamma_{r\mathfrak{y}},
\end{gathered} \tag{11}$$

where

$$\mathfrak{q}_{11} = \mathfrak{q}_{22} = \mathfrak{q}_{33} = \frac{E_c}{(1+\vartheta_c)(1-2\vartheta_c)}, \tag{12}$$

$$\mathfrak{q}_{12} = \mathfrak{q}_{13} = \mathfrak{q}_{23} = \mathfrak{q}_{21} = \mathfrak{q}_{31} = \mathfrak{q}_{32} = \frac{\vartheta_c E_c}{(1+\vartheta_c)(1-2\vartheta_c)},$$

$$\mathfrak{q}_{44c} = \mathfrak{q}_{55c} = \mathfrak{q}_{66c} = \frac{E_c}{2(1+\vartheta_c)}.$$

Additionally, the components of strain would be expressed as (Reddy, 2003)

$$\begin{aligned}
\varepsilon_{\mathfrak{x}\mathfrak{x}} &= \frac{\partial \mathfrak{u}}{\partial \mathfrak{x}},\\
\varepsilon_{\mathfrak{y}\mathfrak{y}} &= \frac{\partial \mathfrak{v}}{\partial \mathfrak{y}},\\
\varepsilon_{\mathfrak{z}\mathfrak{z}} &= \frac{\partial \mathfrak{w}}{\partial \mathfrak{z}},\\
\gamma_{\mathfrak{x}\mathfrak{y}} &= \frac{\partial \mathfrak{u}}{\partial \mathfrak{y}} + \frac{\partial \mathfrak{v}}{\partial \mathfrak{x}},\\
\gamma_{\mathfrak{x}\mathfrak{z}} &= \frac{\partial \mathfrak{u}}{\partial \mathfrak{z}} + \frac{\partial \mathfrak{w}}{\partial \mathfrak{x}},\\
\gamma_{\mathfrak{y}\mathfrak{z}} &= \frac{\partial \mathfrak{v}}{\partial \mathfrak{z}} + \frac{\partial \mathfrak{w}}{\partial \mathfrak{y}}.
\end{aligned} \tag{13}$$

3.2 Hamilton's principle and governing equations

Using Hamilton's principle (Safarpour *et al*. 2025), the problem's basic equations are found in the following variational energy form.

$$\int_{\mathfrak{t}_1}^{\mathfrak{t}_2} \left(\delta \Pi_k - (\delta \Pi_e - \delta \Pi_{\mathfrak{w}})\right) d\mathfrak{t} = 0 \tag{14}$$

The following phrases describe the aforementioned quantities.

$$\Pi_k = \int \left[\rho \left\{\left(\frac{\partial \mathfrak{u}}{\partial \mathfrak{t}}\right)^2 + \left(\frac{\partial \mathfrak{v}}{\partial \mathfrak{t}}\right)^2 + \left(\frac{\partial \mathfrak{w}}{\partial \mathfrak{t}}\right)^2\right\}\right] dV, \tag{15a}$$

$$\Pi_e = \int \left\{\sigma_{\mathfrak{x}\mathfrak{x}}\varepsilon_{\mathfrak{x}\mathfrak{x}} + \sigma_{\mathfrak{y}\mathfrak{y}}\varepsilon_{\mathfrak{y}\mathfrak{y}} + \sigma_{\mathfrak{z}\mathfrak{z}}\varepsilon_{\mathfrak{z}\mathfrak{z}} + \tau_{\mathfrak{y}\mathfrak{z}}\gamma_{\mathfrak{y}\mathfrak{z}} + \tau_{\mathfrak{x}\mathfrak{z}}\gamma_{\mathfrak{x}\mathfrak{z}} + \tau_{\mathfrak{x}\mathfrak{y}}\gamma_{\mathfrak{x}\mathfrak{y}}\right\} dV, \tag{15b}$$

$$\Pi_{\mathfrak{w}} = \frac{1}{2}\int \left\{-K_w \mathfrak{w} + K_p \nabla^2 \mathfrak{w}\right\} \mathfrak{w} dA. \tag{15c}$$

where K_w, and K_p show the Winkler and Pasternak foundations. Eqs. (15a), (15b), and (15c) may be substituted into Eq. (14), and following a mathematical process, the following equations are obtained.

$$\delta \mathfrak{u}_0 : \frac{\partial n_{\mathfrak{x}\mathfrak{x}}}{\partial \mathfrak{x}} + \frac{\partial n_{\mathfrak{x}\mathfrak{y}}}{\partial \mathfrak{y}} = \mathfrak{g}_0 \frac{\partial^2 \mathfrak{u}_0}{\partial \mathfrak{t}^2} + \mathfrak{g}_1 \frac{\partial^2 \mathfrak{u}_1}{\partial \mathfrak{t}^2} + \mathfrak{g}_2 \frac{\partial^2 \mathfrak{u}_2}{\partial \mathfrak{t}^2} + \mathfrak{g}_3 \frac{\partial^2 \mathfrak{u}_3}{\partial \mathfrak{t}^2}, \tag{16a}$$

$$\delta \mathfrak{v}_0 : \frac{\partial n_{\mathfrak{y}\mathfrak{y}}}{\partial \mathfrak{y}} + \frac{\partial n_{\mathfrak{x}\mathfrak{y}}}{\partial \mathfrak{x}} = \mathfrak{g}_0 \frac{\partial^2 \mathfrak{v}_0}{\partial \mathfrak{t}^2} + \mathfrak{g}_1 \frac{\partial^2 \mathfrak{v}_1}{\partial \mathfrak{t}^2} + \mathfrak{g}_2 \frac{\partial^2 \mathfrak{v}_2}{\partial \mathfrak{t}^2} + \mathfrak{g}_3 \frac{\partial^2 \mathfrak{v}_3}{\partial \mathfrak{t}^2}, \tag{16b}$$

$$\delta w_0: \frac{\partial n_{x\zeta}}{\partial x} + \frac{\partial n_{y\zeta}}{\partial y} - K_w\left(w_0 + \left(-\frac{h}{2}\right)w_1 + \left(-\frac{h}{2}\right)^2 w_2 + \left(-\frac{h}{2}\right)^3 w_3\right) + K_p\nabla^2\left(w_0 + \left(-\frac{h}{2}\right)w_1 + \left(-\frac{h}{2}\right)^2 w_2 + \left(-\frac{h}{2}\right)^3 w_3\right) = g_0\frac{\partial^2 w_0}{\partial t^2} + g_1\frac{\partial^2 w_1}{\partial t^2} + g_2\frac{\partial^2 w_2}{\partial t^2} + g_3\frac{\partial^2 w_3}{\partial t^2}, \tag{16c}$$

$$\delta u_1: \frac{\partial m_{xx}}{\partial x} + \frac{\partial m_{xy}}{\partial y} - n_{x\zeta} = g_1\frac{\partial^2 u_0}{\partial t^2} + g_2\frac{\partial^2 u_1}{\partial t^2} + g_3\frac{\partial^2 u_2}{\partial t^2} + g_4\frac{\partial^2 u_3}{\partial t^2}, \tag{16d}$$

$$\delta v_1: \frac{\partial m_{yy}}{\partial y} + \frac{\partial m_{xy}}{\partial x} - n_{y\zeta} = g_1\frac{\partial^2 v_0}{\partial t^2} + g_2\frac{\partial^2 v_1}{\partial t^2} + g_3\frac{\partial^2 v_2}{\partial t^2} + g_4\frac{\partial^2 v_3}{\partial t^2}, \tag{16e}$$

$$\delta w_1: \frac{\partial m_{x\zeta}}{\partial x} + \frac{\partial m_{y\zeta}}{\partial y} - n_{\zeta\zeta} + \left(-\frac{h}{2}\right)\left(-K_w\left(w_0 + \left(-\frac{h}{2}\right)w_1 + \left(-\frac{h}{2}\right)^2 w_2 + \left(-\frac{h}{2}\right)^3 w_3\right) + K_p\nabla^2\left(w_0 + \left(-\frac{h}{2}\right)w_1 + \left(-\frac{h}{2}\right)^2 w_2 + \left(-\frac{h}{2}\right)^3 w_3\right)\right) = g_1\frac{\partial^2 w_0}{\partial t^2} + g_2\frac{\partial^2 w_1}{\partial t^2} + g_3\frac{\partial^2 w_2}{\partial t^2} + g_4\frac{\partial^2 w_3}{\partial t^2}, \tag{16f}$$

$$\delta u_2: \frac{\partial p_{xx}}{\partial x} + \frac{\partial p_{xy}}{\partial y} - 2m_{x\zeta} = g_2\frac{\partial^2 u_0}{\partial t^2} + g_3\frac{\partial^2 u_1}{\partial t^2} + g_4\frac{\partial^2 u_2}{\partial t^2} + g_5\frac{\partial^2 u_3}{\partial t^2}, \tag{16g}$$

$$\delta v_2: \frac{\partial p_{yy}}{\partial y} + \frac{\partial p_{xy}}{\partial x} + -2m_{y\zeta} = g_2\frac{\partial^2 v_0}{\partial t^2} + g_3\frac{\partial^2 v_1}{\partial t^2} + g_4\frac{\partial^2 v_2}{\partial t^2} + g_5\frac{\partial^2 v_3}{\partial t^2}, \tag{16h}$$

$$\delta w_2: \frac{\partial p_{x\zeta}}{\partial x} + \frac{\partial p_{y\zeta}}{\partial y} - 2m_{\zeta\zeta} + \left(-\frac{h}{2}\right)^2\left(-K_w\left(w_0 + \left(-\frac{h}{2}\right)w_1 + \left(-\frac{h}{2}\right)^2 w_2 + \left(-\frac{h}{2}\right)^3 w_3\right) + K_p\nabla^2\left(w_0 + \left(-\frac{h}{2}\right)w_1 + \left(-\frac{h}{2}\right)^2 w_2 + \left(-\frac{h}{2}\right)^3 w_3\right)\right) = g_2\frac{\partial^2 w_0}{\partial t^2} + g_3\frac{\partial^2 w_1}{\partial t^2} + g_4\frac{\partial^2 w_2}{\partial t^2} + g_5\frac{\partial^2 w_3}{\partial t^2}, \tag{16i}$$

$$\delta u_3: \frac{\partial q_{xx}}{\partial x} + \frac{\partial q_{xy}}{\partial y} - 3p_{x\zeta} = g_3\frac{\partial^2 u_0}{\partial t^2} + g_4\frac{\partial^2 u_1}{\partial t^2} + g_5\frac{\partial^2 u_2}{\partial t^2} + g_6\frac{\partial^2 u_3}{\partial t^2}, \tag{16j}$$

$$\delta v_3: \frac{\partial q_{yy}}{\partial y} + \frac{\partial q_{xy}}{\partial x} - 3p_{y\zeta} = g_3\frac{\partial^2 v_0}{\partial t^2} + g_4\frac{\partial^2 v_1}{\partial t^2} + g_5\frac{\partial^2 v_2}{\partial t^2} + g_6\frac{\partial^2 v_3}{\partial t^2}, \tag{16k}$$

$$\delta w_3: \frac{\partial q_{x\zeta}}{\partial x} + \frac{\partial q_{y\zeta}}{\partial y} - 3p_{\zeta\zeta} + \left(-\frac{h}{2}\right)^3\left(-K_w\left(w_0 + \left(-\frac{h}{2}\right)w_1 + \left(-\frac{h}{2}\right)^2 w_2 + \left(-\frac{h}{2}\right)^3 w_3\right) + K_p\nabla^2\left(w_0 + \left(-\frac{h}{2}\right)w_1 + \left(-\frac{h}{2}\right)^2 w_2 + \left(-\frac{h}{2}\right)^3 w_3\right)\right) = g_3\frac{\partial^2 w_0}{\partial t^2} + g_4\frac{\partial^2 w_1}{\partial t^2} + g_5\frac{\partial^2 w_2}{\partial t^2} + g_6\frac{\partial^2 w_3}{\partial t^2}, \tag{16l}$$

In which:

$$\{n_{xx}, m_{xx}, p_{xx}, q_{xx}\} = \int\{1, \zeta, \zeta^2, \zeta^3\}\sigma_{xx}d\zeta, \tag{17}$$

$$\{n_{\mathfrak{yy}}, m_{\mathfrak{yy}}, p_{\mathfrak{yy}}, q_{\mathfrak{yy}}\} = \int\{1, \mathfrak{z}, \mathfrak{z}^2, \mathfrak{z}^3\}\sigma_{\mathfrak{yy}}d\mathfrak{z},$$

$$\{n_{\mathfrak{zz}}, m_{\mathfrak{zz}}, p_{\mathfrak{zz}}, q_{\mathfrak{zz}}\} = \int\{1, \mathfrak{z}, \mathfrak{z}^2, \mathfrak{z}^3\}\sigma_{\mathfrak{zz}}d\mathfrak{z},$$

$$\{n_{\mathfrak{xy}}, m_{\mathfrak{xy}}, p_{\mathfrak{xy}}, q_{\mathfrak{xy}}\} = \int\{1, \mathfrak{z}, \mathfrak{z}^2, \mathfrak{z}^3\}\tau_{\mathfrak{xy}}d\mathfrak{z},$$

$$\{n_{\mathfrak{yz}}, m_{\mathfrak{yz}}, p_{\mathfrak{yz}}, q_{\mathfrak{yz}}\} = \int\{1, \mathfrak{z}, \mathfrak{z}^2, \mathfrak{z}^3\}\tau_{\mathfrak{yz}}d\mathfrak{z},$$

$$\{n_{\mathfrak{xz}}, m_{\mathfrak{xz}}, p_{\mathfrak{xz}}, q_{\mathfrak{xz}}\} = \int\{1, \mathfrak{z}, \mathfrak{z}^2, \mathfrak{z}^3\}\tau_{\mathfrak{xz}}d\mathfrak{z},$$

$$\{\mathfrak{g}_0, \mathfrak{g}_1, \mathfrak{g}_2, \mathfrak{g}_3, \mathfrak{g}_4, \mathfrak{g}_5, \mathfrak{g}_6\} = \int\{1, \mathfrak{z}, \mathfrak{z}^2, \mathfrak{z}^3, \mathfrak{z}^4, \mathfrak{z}^5, \mathfrak{z}^6\}\rho d\mathfrak{z}.$$

Also, general boundary conditions can be given by:

$$\begin{aligned}
&\delta\mathfrak{u}_0: \quad (n_{\mathfrak{xx}})\hat{n}_{\mathfrak{x}} + (n_{\mathfrak{xy}})\hat{n}_{\mathfrak{y}} = 0,\\
&\delta\mathfrak{v}_0: \quad (n_{\mathfrak{xy}})\hat{n}_{\mathfrak{x}} + (n_{\mathfrak{yy}})\hat{n}_{\mathfrak{y}} = 0,\\
&\delta\mathfrak{w}_0: \quad (n_{\mathfrak{xz}})\hat{n}_{\mathfrak{x}} + (n_{\mathfrak{yz}})\hat{n}_{\mathfrak{y}} = 0,\\
&\delta\mathfrak{u}_1: \quad (m_{\mathfrak{xx}})\hat{n}_{\mathfrak{x}} + (m_{\mathfrak{xy}})\hat{n}_{\mathfrak{y}} = 0,\\
&\delta\mathfrak{v}_1: \quad (m_{\mathfrak{xy}})\hat{n}_{\mathfrak{x}} + (m_{\mathfrak{yy}})\hat{n}_{\mathfrak{y}} = 0,\\
&\delta\mathfrak{w}_1: \quad (m_{\mathfrak{xz}})\hat{n}_{\mathfrak{x}} + (m_{\mathfrak{yz}})\hat{n}_{\mathfrak{y}} = 0,\\
&\delta\mathfrak{u}_2: \quad (p_{\mathfrak{xx}})\hat{n}_{\mathfrak{x}} + (p_{\mathfrak{xy}})\hat{n}_{\mathfrak{y}} = 0,\\
&\delta\mathfrak{v}_2: \quad (p_{\mathfrak{xy}})\hat{n}_{\mathfrak{x}} + (p_{\mathfrak{yy}})\hat{n}_{\mathfrak{y}} = 0,\\
&\delta\mathfrak{w}_2: \quad (p_{\mathfrak{xz}})\hat{n}_{\mathfrak{x}} + (p_{\mathfrak{yz}})\hat{n}_{\mathfrak{y}} = 0,\\
&\delta\mathfrak{u}_3: \quad (q_{\mathfrak{xx}})\hat{n}_{\mathfrak{x}} + (q_{\mathfrak{xy}})\hat{n}_{\mathfrak{y}} = 0,\\
&\delta\mathfrak{v}_3: \quad (q_{\mathfrak{xy}})\hat{n}_{\mathfrak{x}} + (q_{\mathfrak{yy}})\hat{n}_{\mathfrak{y}} = 0,\\
&\delta\mathfrak{w}_3: \quad (q_{\mathfrak{xz}})\hat{n}_{\mathfrak{x}} + (q_{\mathfrak{yz}})\hat{n}_{\mathfrak{y}} = 0,
\end{aligned} \tag{18}$$

4. Numerical solution

To deal with the produced governing equations, the study applies the differential quadrature method (DQM). The predicted values of the mth and nth derivative functions with respect to $\mathfrak{x}$ and $\mathfrak{y}$ are given by the DQM (Bert *et al*. 1996, Safarpour *et al*. 2021b):

$$\begin{aligned}
\mathfrak{f}_{\mathfrak{x}}^{(m)}(\mathfrak{x}_i,\mathfrak{y}_i) &= \sum_{k=1}^{n_{\mathfrak{x}}} \mathfrak{a}_{ik}^{(m)}\mathfrak{f}(\mathfrak{x}_k,\mathfrak{y}_i),\\
\mathfrak{f}_{\mathfrak{y}}^{(n)}(\mathfrak{x}_i,\mathfrak{y}_i) &= \sum_{l=1}^{n_{\mathfrak{y}}} \mathfrak{b}_{jl}^{(n)}\mathfrak{f}(\mathfrak{x}_i,\mathfrak{y}_l),\\
\mathfrak{f}_{\mathfrak{x}\mathfrak{y}}^{(m+n)}(\mathfrak{x}_i,\mathfrak{y}_i) &= \sum_{k=1}^{n_{\mathfrak{x}}} \sum_{l=1}^{n_{\mathfrak{y}}} \mathfrak{a}_{ik}^{(m)}\mathfrak{b}_{jl}^{(n)}\mathfrak{f}(\mathfrak{x}_k,\mathfrak{y}_l),
\end{aligned} \tag{19}$$

The weighting coefficients $\mathfrak{a}_{ij}^{(m)}$ and $\mathfrak{b}_{ij}^{(n)}$ are, where $n_{\mathfrak{x}}$ and $n_{\mathfrak{y}}$ stand for the number of points along the $\mathfrak{x}$ and $\mathfrak{y}$ directions, respectively.

$$\begin{aligned}
\mathfrak{a}_{ij}^{(1)} &= \frac{\pi(\mathfrak{x}_i)}{(\mathfrak{x}_i-\mathfrak{x}_j)\pi(\mathfrak{x}_j)}, i,j = 1,2,\cdots n_{\mathfrak{x}}, i \neq j,\\
\mathfrak{b}_{ij}^{(1)} &= \frac{\pi(\mathfrak{y}_i)}{(\mathfrak{y}_i-\mathfrak{y}_j)\pi(\mathfrak{y}_j)}, i,j = 1,2,\cdots n_{\mathfrak{y}}, i \neq j.
\end{aligned} \tag{20}$$

where

$$\begin{aligned}
\pi(\mathfrak{x}_i) &= \prod_{j=1}^{n_{\mathfrak{x}}}(\mathfrak{x}_i-\mathfrak{x}_j),\\
\pi(\mathfrak{y}_i) &= \prod_{j=1}^{n_{\mathfrak{y}}}(\mathfrak{y}_i-\mathfrak{y}_j).
\end{aligned} \tag{21}$$

and when $i = j$

$$\begin{aligned}
\mathfrak{a}_{ij}^{(1)} = \mathfrak{a}_{ii}^{(1)} &= -\sum_{k=1}^{n_{\mathfrak{x}}} \mathfrak{a}_{ik}^{(1)}, i = 1,2,\cdots n_{\mathfrak{x}}, i \neq k, i = j,\\
\mathfrak{b}_{ij}^{(1)} = \mathfrak{b}_{ii}^{(1)} &= -\sum_{k=1}^{n_{\mathfrak{x}}} \mathfrak{b}_{il}^{(1)}, i = 1,2,\cdots n_{\mathfrak{y}}, i \neq l, i = j.
\end{aligned} \tag{22}$$

The following is the expression for the weighting coefficients with high-order derivatives.

$$\begin{aligned}
\mathfrak{a}_{ij}^{(2)} &= \sum_{k=1}^{n_{\mathfrak{x}}} \mathfrak{a}_{ik}^{(1)}\mathfrak{a}_{kj}^{(1)}, \mathfrak{a}_{ij}^{(3)} = \sum_{k=1}^{n_{\mathfrak{x}}} \mathfrak{a}_{ik}^{(1)}\mathfrak{a}_{kj}^{(2)}, \mathfrak{a}_{ij}^{(4)} = \sum_{k=1}^{n_{\mathfrak{x}}} \mathfrak{a}_{ik}^{(1)}\mathfrak{a}_{kj}^{(3)},\\
\mathfrak{b}_{ij}^{(2)} &= \sum_{l=1}^{n_{\mathfrak{y}}} \mathfrak{b}_{il}^{(1)}\mathfrak{b}_{lj}^{(1)}, \mathfrak{b}_{ij}^{(3)} = \sum_{l=1}^{n_{\mathfrak{y}}} \mathfrak{b}_{il}^{(1)}\mathfrak{b}_{lj}^{(2)}, \mathfrak{b}_{ij}^{(4)} = \sum_{l=1}^{n_{\mathfrak{y}}} \mathfrak{b}_{il}^{(1)}\mathfrak{b}_{lj}^{(3)}.
\end{aligned} \tag{23}$$

The Chebyshev–Gauss–Lobatto interpolation method is used in this investigation. Consequently, the locations of these interpolations in the present study are

$$\begin{aligned}
\mathfrak{x}_i &= \frac{a}{2}\left[1-\cos\frac{(i-1)\pi}{(n_{\mathfrak{x}}-1)}\right], i = 1,2,\cdots n_{\mathfrak{x}},\\
\mathfrak{y}_i &= \frac{b}{2}\left[1-\cos\frac{(i-1)\pi}{(n_{\mathfrak{y}}-1)}\right], i = 1,2,\cdots n_{\mathfrak{y}}.
\end{aligned} \tag{24}$$

For displacement fields we have:

$$\mathfrak{u}_B(\mathfrak{x},\mathfrak{y},\mathfrak{t}) = \bar{\mathfrak{u}}_B(\mathfrak{x},\mathfrak{y})e^{i\Omega\mathfrak{t}} \tag{25}$$

$$\mathfrak{v}_B(\mathfrak{x},\mathfrak{y},\mathfrak{t}) = \bar{\mathfrak{v}}_B(\mathfrak{x},\mathfrak{y})e^{i\Omega \mathfrak{t}}$$

$$\mathfrak{w}_B(\mathfrak{x},\mathfrak{y},\mathfrak{t}) = \bar{\mathfrak{w}}_B(\mathfrak{x},\mathfrak{y})e^{i\Omega \mathfrak{t}}$$

where Ω is the system's natural frequency, $i = \sqrt{1}$, and $B = 0,1,2,3$. Eqs. (17), (19), and (25) may be substituted into Eq. (16a-l) while taking into account different boundary conditions (Eq. (18)).

$$([\mathbb{K}] - [\mathbb{M}]\Omega^2)\{\mathbb{X}\} = 0$$
$$\{\mathbb{X}\}^T = \{\bar{\mathfrak{u}}_0 \ \bar{\mathfrak{v}}_0 \ \bar{\mathfrak{w}}_0 \ \bar{\mathfrak{u}}_1 \ \bar{\mathfrak{v}}_1 \ \bar{\mathfrak{w}}_1 \ \bar{\mathfrak{u}}_2 \ \bar{\mathfrak{v}}_2 \ \bar{\mathfrak{w}}_2 \ \bar{\mathfrak{u}}_3 \ \bar{\mathfrak{v}}_3 \ \bar{\mathfrak{w}}_3\} \tag{26}$$

where the mass matrix and stiffness are indicated by $[\mathbb{K}]$, and $[\mathbb{M}]$. Additionally, the system's natural frequency may be found by solving Eq. (26). For ease of use, dimensionless quantities are defined as follows:

$$\bar{\Omega} = \Omega\sqrt{\frac{\rho_m}{E_m}}, \quad \overline{K}_w = \frac{K_w a^4}{D_m}, \ \overline{K}_p = \frac{K_p a^2}{D_m}, \ D_m = \frac{E_m h^3}{12(1-\nu_m^2)} \tag{27}$$

5. Result

5.1 Validation

Table 1 shows a comparison of the dimensionless fundamental frequency for functionally graded graphene platelets (GPLs)-reinforced plates, material properties, and reinforcement orientations being the basis. The results from the table relate to comparing the values obtained from the current study with those given in a previous Ref. (Song *et al*. 2017). The dimensionless frequency is indicated for three different combinations of materials: Pure Epoxy, GPL-UD (unidirectional), and GPL-X (cross-ply). For the Pure Epoxy configuration, the reference and present study frequency values are nearly the same, with the reference providing a value of 0.0584 and the present study offering 0.0582. Likewise, concerning the GPL-UD configuration, the reference gives a frequency of 0.1216, whilst the present study is 0.1213, which shows a slight variation. The largest difference is found in the GPL-X configuration, where the reference gives a value of 0.1378, and the present study gives a slightly lower value of 0.1375. The results indicate the present study's findings to be in close agreement with the reference data, and the minor variations are likely due to differences in the modeling or computational methods. Such verification is an assurance of the current study's approach being reliable and supports its validity in predicting the vibrational characteristics of functionally graded GPLs-reinforced plates.

5.2 Parametric study

Fig. 4 analyzes the change of the dimensionless basic natural frequency, depending on the mixed composite reinforcement's weight fraction in the reinforcement materials. The graphs represent the three boundary conditions: CCCC (all edges clamped), SSSS (all edges simply supported), and CSCS (two opposite edges clamped, two opposite edges simply supported). The x-axis indicates the weight fraction of the RCA and UFA mixture, while the y-axis shows the dimensionless natural frequency. The results indicate a trend that as the weight of RCA + UFA rises, the dimensionless

Table 1 A comparison study for dimensionless fundamental frequency $\bar{\Omega} = \Omega h\sqrt{\rho_M/E_M}$ of a functionally graded GPLs-reinforced plate

Source	Pure epoxy	GPL-UD	GPL-X
Ref. (Song *et al*. 2017)	0.0584	0.1216	0.1378
Present	0.0582	0.1213	0.1375

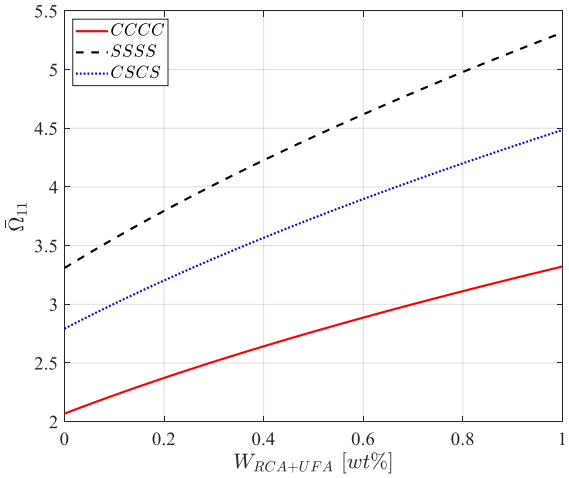

Fig. 4 The change of the dimensionless basic natural frequency, depending on the mixed composite reinforcement's weight fraction in the reinforcement materials

frequency also increases for every boundary condition, and the increase of the clamped condition (CCCC) is the highest. This points to the conclusion that RCA + UFA mixing improves the vibrational performance of the reinforced structure with different boundary conditions, having different degrees of affecting the structural response. The findings underline the significance of boundary conditions in the dynamic characteristics of the plate induction.

Fig. 5 delves into the relationship between various types of reinforcement materials and the non-dimensional fundamental natural frequency based on the RCA+UFA weight fraction. In this case, the three reinforcement patterns—Pattern X, Pattern O, and Pattern UD—are evaluated. The x-axis again measures the fraction of RCA+UFA by weight, while the y-axis represents the non-dimensional natural frequency. The natural frequency again increases as RCA+UFA fractionation rises, as is the case in the first diagram. The "Pattern X" configuration is the one that exhibits the highest natural frequency increase, followed next by "Pattern UD" and "Pattern O", which show a slowing in increase. The above indicates that the arrangement of the reinforcement material has a decisive influence on the dynamic properties of the entire structure. The variation in the response under different reinforcement patterns points out that the right choice of material composition is crucial for achieving the best dynamic performance of the reinforced structure.

Fig. 6 investigates how the aspect ratio a/h (with a being the length and h being the height) influences the dimensionless fundamental natural frequency. Three aspect ratios under consideration are $a/h = 30$, $a/h = 35$, and $a/h = 40$. A gradual increase of RCA+UFA weight fraction results in the natural frequency rise for all the aspect ratios. On the other hand, the slower aspect ratio case

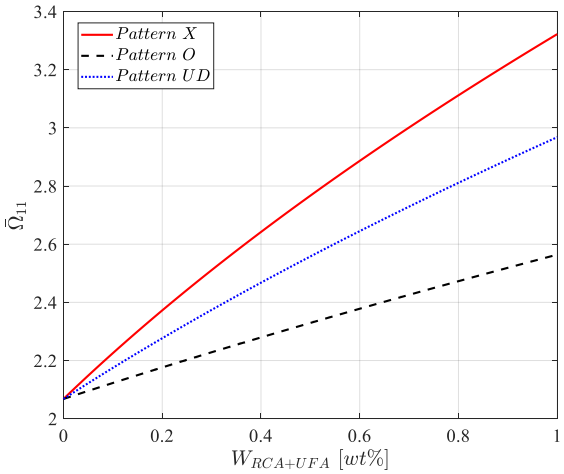

Fig. 5 The relationship between various types of reinforcement materials and the non-dimensional fundamental natural frequency based on the RCA+UFA weight fraction

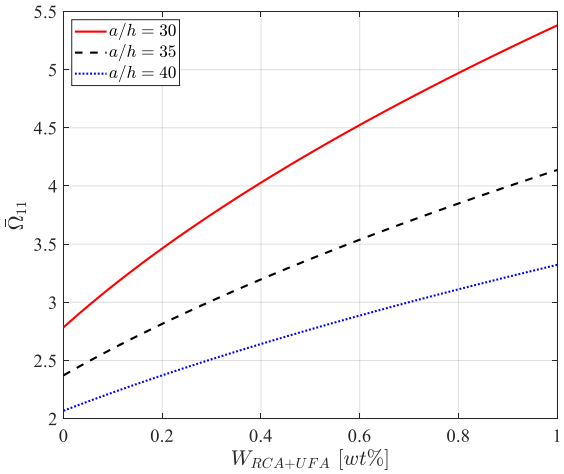

Fig. 6 The relationship between a/h ratio and the non-dimensional fundamental natural frequency based on the RCA+UFA weight fraction

that is $a/h = 30$ also has the frequency rising at a higher rate compared to the other two. The pattern infers that with a higher length-to-height ratio, the changes in material composition have a lesser effect on the dynamic response. Moreover, the results point out that the choice of aspect ratio for the structure plays a significant role in obtaining the specific vibrational characteristics and, consequently, the enhancement of overall structural integrity and performance.

Fig. 7 shows how the b/a ratio affects the dimensionless natural frequency, which is plotted against the weight percentage of RCA+UFA. The three ratios compared are $b/a = 1$, $b/a = 2$, and $b/a = 3$. The results indicate a general tendency for the natural frequency to get higher with increased RCA+UFA content, and the increase is most noticeable for $b/a = 1$. The smaller the

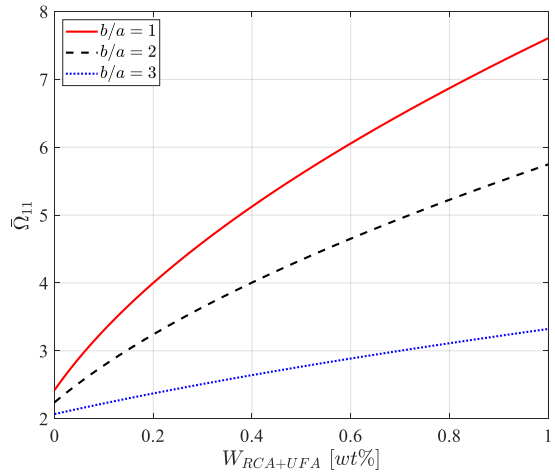

Fig. 7 The relationship between b/a ratio and the non-dimensional fundamental natural frequency based on the RCA+UFA weight fraction

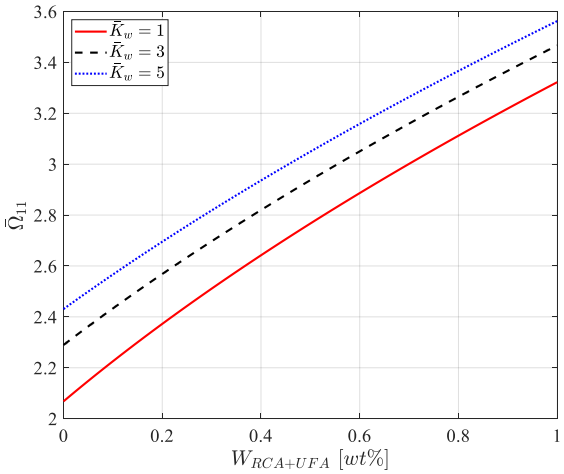

Fig. 8 The relationship between $\overline{K}_w$ parameter and the non-dimensional fundamental natural frequency based on the RCA+UFA weight fraction

width-to-length ratio, the more rapidly the increase in frequency is. This indicates that the plate geometry, particularly the width-to-length ratio, plays a major role in the vibrational characteristics. These results imply that the structural dynamic response can still be enhanced by combining the right geometric proportions with the appropriate material reinforcement composition.

Fig. 8 depicts how the dimensionless fundamental natural frequency changes with the weight fraction of the RCA+UFA mixture for different values of the Winkler foundation coefficient $\overline{K}_w$. The variation of the Winkler foundation coefficient $\overline{K}_w$ is restricted to three values: $\overline{K}_w$=1, $\overline{K}_w$=3, and $\overline{K}_w$=5. The x-axis shows the RCA+UFA mixture's weight fraction, while the y-axis shows the dimensionless fundamental natural frequency. The plot indicates that all $\overline{K}_w$ values exhibit an

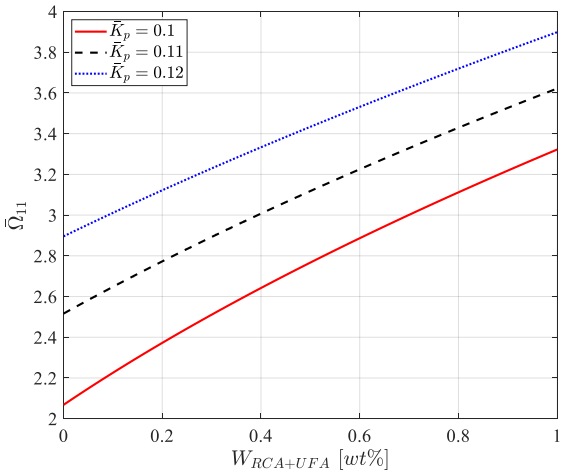

Fig. 9 The relationship between the Pasternak foundation coefficient $\overline{K}_p$ and the dimensionless fundamental natural frequency, along with different weight fractions of RCA+UFA mixture

elevation in the dimensionless natural frequency corresponding to an increase in W_(RCA+UFA). What catches the eye is that the frequency goes up considerably when the Winkler foundation coefficient $\overline{K}_w$ is at its lowest (for $\overline{K}_w$=1), which means that a softer ground makes the mixture of the reinforcement materials more sensitive and hence leading to a higher frequency. The dynamic characteristics of the structure vs rely primarily on foundation stiffness, which is why higher $\overline{K}_w$ values cause lower natural frequency increases to occur with rising reinforcement ratios. Thus, this finding highlights the role played by the foundation's stiffness in determining the behavior of the structure.

Fig. 9 shows the relationship between the Pasternak foundation coefficient $\overline{K}_p$ and the dimensionless fundamental natural frequency, along with different weight fractions of RCA+UFA mixture. The coefficients considered are three: $\overline{K}_p$=0.1, $\overline{K}_p$=0.11, and $\overline{K}_p$=0.12. The weight fraction of the RCA+UFA mixture is again represented on the x-axis, while the y-axis indicates the dimensionless fundamental natural frequency. The same trend is seen in this plot as well, the frequency increases with an increase in weight fraction of the RCA+UFA mixture. The natural frequency also increases appreciably at the $\overline{K}_p$ low values. The higher the $\overline{K}_p$ value, the slower the natural frequency increases, which implies a damping effect of the Pasternak foundation on the vibration response. With this plot, it is possible to see that by changing the foundation's stiffness, the $\overline{K}_p$, one can change the dynamic characteristics of the plate, with the case of stiff foundations being less responsive to alterations in the reinforcement mixture.

Fig. 10 shows the relationship between the dimensionless fundamental natural frequency and the Winkler foundation coefficient $\overline{K}_w$ for different types of boundary conditions (CCCC, SSSS, CSCS). The $\overline{K}_w$ value is displayed on the x-axis and the dimensionless natural frequency is indicated on the y-axis. It can be seen from the plot that there is an increase in the frequency for all cases when $\overline{K}_w$ is increased. The interaction of the boundary conditions causes the increase in frequency to differ: CCCC (all edges clamped) shows a larger increase than SSSS (all edges simply

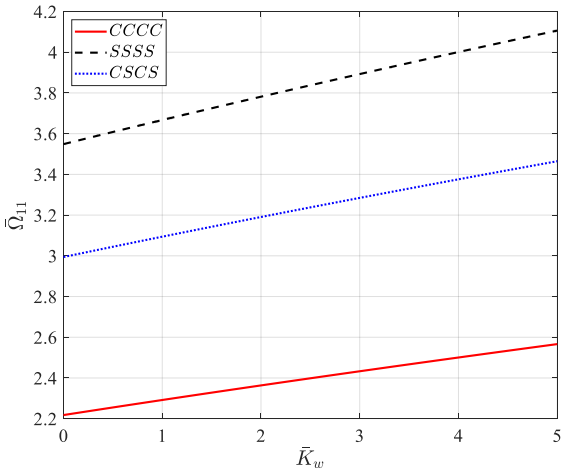

Fig. 10 The relationship between the dimensionless fundamental natural frequency and the Winkler foundation coefficient $\overline{K}_w$ for different types of boundary conditions

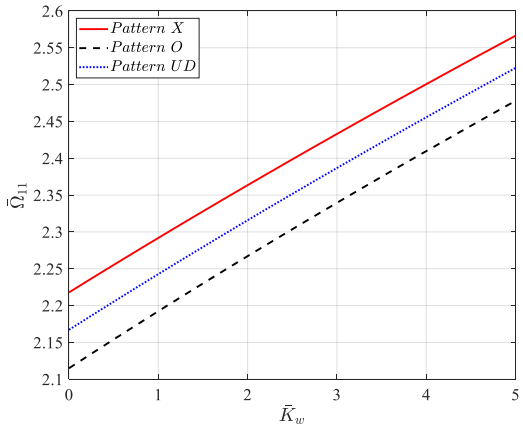

Fig. 11 The relationship between the Winkler foundation coefficient $\overline{K}_w$ and the dimensionless natural frequency under three different types of reinforcement materials

supported) and CSCS (two edges clamped and two edges simply supported) cases. Therefore, it can be concluded that the boundary condition has a strong influence over the dynamic behavior of the plate, as clamped edges lead to a more substantial rise in natural frequency. The inquiry substantiates the notion that both the foundation and the boundary conditions need to be incorporated into the consideration of structural vibration analysis.

Fig. 11 investigates the relationship between the Winkler foundation coefficient $\overline{K}_w$ and the dimensionless natural frequency under three different types of reinforcement materials: Pattern X, Pattern O, and Pattern UD. The x-axis depicts the value of $\overline{K}_w$ and the y-axis indicates the dimensionless fundamental natural frequency. The results show that up to $\overline{K}_w$ all patterns' natural frequency went up, with Pattern X showing the highest followed by Pattern O and then Pattern UD

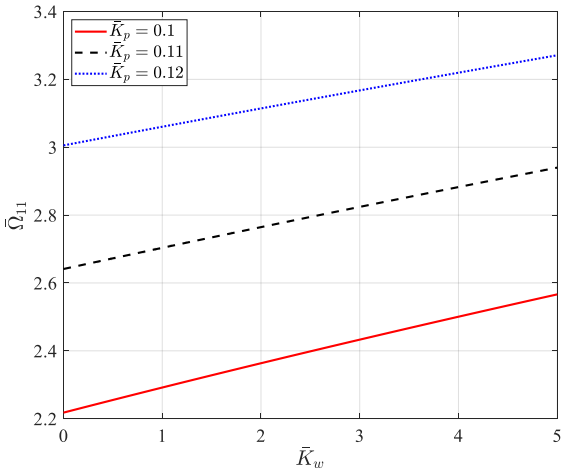

Fig. 12 The relationship between the Winkler foundation coefficient and the dimensionless natural frequency under three different values of $\overline{K}_P$ parameters

showing the lowest increase. This implies that the type of reinforcement material has a major role in the structural performance, with some ones showing higher efficiency in reinforcing than others. The graph shows the sophisticated interdependence of foundation stiffness and reinforcement pattern with respect to the optimization of the dynamic characteristics of the reinforced structures, thus pointing out the necessity of proper material and design selection even more.

Fig. 12 illustrates how the dimensionless fundamental natural frequency changes with the Winkler foundation coefficient $\overline{K}_w$ for three values of the Pasternak foundation coefficient $\overline{K}_p$: $\overline{K}_p$=0.1, $\overline{K}_p$=0.11, and $\overline{K}_p$=0.12. The Winkler foundation coefficient $\overline{K}_w$ is plotted on the x-axis while the dimensionless natural frequency is plotted on the y-axis. According to the data, an increase in the Winkler coefficient $\overline{K}_w$ also causes an increase in the natural frequency of all $\overline{K}_p$ values. Nevertheless, the increase's slope is more pronounced for lower $\overline{K}_p$ value (i.e., $\overline{K}_p$=0.1) than for higher $\overline{K}_p$ values, which means that the plate's dynamic response is more sensitive to $\overline{K}_w$ changes when the Pasternak foundation is not very stiff. This means that the Pasternak foundation acts like a tuning element that controls the vibrational behavior of the structure, leading to stiffer foundations (higher $\overline{K}_p$) producing a slow increase in the frequency of the natural vibration. The interaction between the Winkler and Pasternak foundation coefficients is pivotal in defining the vibrational characteristics of the plate.

Fig. 13 shows the relationship between the dimensionless fundamental natural frequency (y-axis) and the Winkler foundation coefficient $\overline{K}_w$ (x-axis), with aspect ratio a/h as a parameter. The aspect ratios $a/h = 30$, $a/h = 35$, and $a/h = 40$ are considered. The plot demonstrates that with increasing $\overline{K}_w$, the natural frequency increases for every aspect ratio. The plate with a lower aspect ratio ($a/h = 30$) shows a higher increase in natural frequency than the plates with higher aspect ratios ($a/h = 35$ and $a/h = 40$) do. This implies that the dynamic response of the plate is less affected by foundation stiffness when the width- to-height ratio is more significant. The findings highlight the role of the aspect ratio in determining the structural dynamic behavior, with smaller

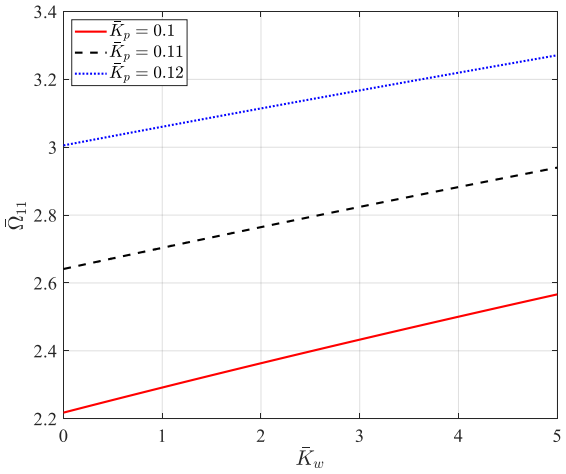

Fig. 13 The relationship between the dimensionless fundamental natural frequency and the Winkler foundation coefficient $\overline{K}_w$, with aspect ratio a/h as a parameter

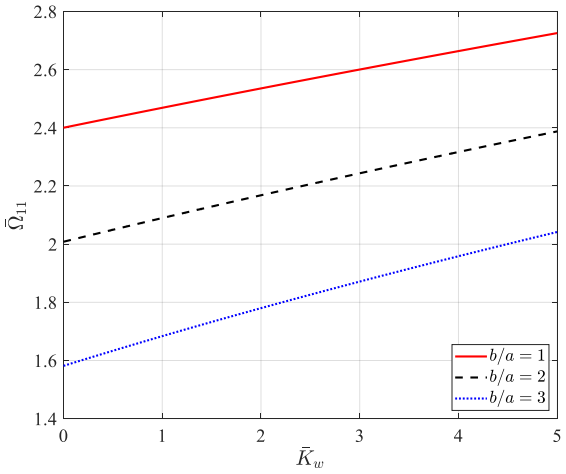

Fig. 14 An analysis of the Winkler foundation coefficient effect on the dimensionless natural frequency in relation to the plate's varying width-to-length ratios

ratios allowing for a more considerable effect of the stiffness of the foundation on the natural frequency.

Fig. 14 provides an analysis of the Winkler foundation coefficient $\overline{K}_w$ effect on the dimensionless natural frequency in relation to the plate's varying width-to-length ratios, specifically $b/a = 1$, $b/a = 2$, and $b/a = 3$. On the x-axis is $\overline{K}_w$, while the y-axis represents the dimensionless natural frequency. The graph depicts that for all b/a values, the natural frequency rises with the increase of $\overline{K}_w$. Nonetheless, the higher the width-to-length ratio, the slower the natural frequency increase becomes. Most notably, for the $b/a = 1$ case, the fastest rate of natural frequency increase occurs, while the slowest is for the $b/a = 3$ case. This hints that the plate

geometry, particularly the width-to-length ratio, is one of the factors that govern the sensitivity of the dynamic response of the plate to variations in the foundation stiffness. The findings stress the necessity of considering the role of geometric factors in the context of structural dynamic behavior and the importance of their optimization in design.

6. Conclusions

The current research offers a thorough method for maximizing the performance of structures with RCA and UFA by concentrating on the vibration characteristics of the plate structures resting on a Winkler-Pasternak elastic foundation. The introduction of HSDT brings about a profound representation of the dynamic behavior of reinforced concrete structures by taking into account the complicated interactions of transverse shear deformation and rotational inertia. Using Hamilton's principle, the governing equations of motion are derived while accounting for the interaction between the material properties, boundary conditions, and the elastic foundation. The factorial design approach applied in this research provides a detailed procedure for the assessment of the various combinations of RCA and UFA on structural performance, thereby calling attention to the need for optimizing material mixtures in order to achieve minimum vibrations and a higher degree of structural stability. The employment of the DQM with high-order derivatives and weighting coefficients allows one to obtain very accurate numerical solutions, thus making sure that the dynamic response of the plate is correctly simulated. Moreover, the Chebyshev–Gauss–Lobatto interpolation method contributes to the numerical precision and computational efficiency, thereby rendering the proposed framework both strong and suitable for industrial applications. The findings indicate that the combinations of RCA and UFA have a considerable effect on the natural frequencies and the vibrational characteristics of the plate, hence, it can be concluded that by rightly choosing these materials, better performance with lower vibrations and longer structure life can be obtained. In terms of sustainability, this research reveals that the use of RCA and UFA not only helps to recycle the industrial by-products but also aids the production of top-quality, green building materials. The optimization framework proposed in this paper allows for designing stronger, more resource-efficient concrete structures, thus matching the increasing need for sustainable solutions in engineering. Future studies should aim at developing this method for other types of structural parts and investigating other material combinations to make this method more widely applicable in actual engineering projects. Eventually, this research paves the way for adopting sustainable material practices in civil engineering, thus pulling up the curtain on environmentally friendly and cost-effective construction technologies.

Acknowledgement

This research is funded by INTI International University.

References

Abdelmadjid, M., El Sallah, Z.M., Yaylaci, M., Djafar, A.K., Ali, B., Abdelghani, B., Ozturk, S., Ozdemir, M.E. and Yaylaci, E.U. (2024), "Effects of the stiffness of an inclusion on the mechanical behavior of an aluminum alloy plate with a lateral notch", *Steel Compos. Struct.*, **51**(1), 63.

https://doi.org/10.12989/scs.2024.51.1.063
Abdelmalek, A., Bouazza, M., Zidour, M. and Benseddiq, N. (2019), "Hygrothermal effects on the free vibration behavior of composite plate using n th-order shear deformation theory: a micromechanical approach", *Iran. J. Sci. Tech. Transact. Mech. Eng.*, **43**, 61-73. https://doi.org/10.1007/s40997-017-0140-y
Abderezak, R., Rabia, B., Daouadji, T.H., Abbes, B., Belkacem, A. and Abbes, F. (2018), "Elastic analysis of interfacial stresses in prestressed PFGM-RC hybrid beams", *Adv. Mater. Res.*, **7**(2), 83. https://doi.org/10.12989/amr.2018.7.2.083
Abderezak, R., Daouadji, T.H. and Rabia, B. (2021), "Aluminum beam reinforced by externally bonded composite materials", *Adv. Mater. Res.*, **10**(1), 23-44. https://doi.org/10.12989/amr.2021.10.1.023
Abualnour, M., Chikh, A., Hebali, H., Kaci, A., Tounsi, A., Bousahla, A.A. and Tounsi, A. (2019), "Thermomechanical analysis of antisymmetric laminated reinforced composite plates using a new four variable trigonometric refined plate theory", *Comput. Concr.*, **24**, 489-498. https://doi.org/10.12989/cac.2019.24.6.489
Achache, H., Abdi, G., El Sallah, Z.M., Yaylaci, M., Boughedaoui, R., Ozturk, S., Yaylaci, E.U. and Ozdemir, M.E. (2025), "Numerical analysis of three-point bending of sandwich panels with different core cross-sections: Finite element study", *Adv. Nano Res.*, **18**(5), 481-488. https://doi.org/10.12989/anr.2025.18.5.481
Adeniyi, A.G., Abdulkareem, S.A., Iwuozor, K.O., Abdulkareem, M.T., Adeyanju, C.A., Emenike, E.C., Ndagi, M. and Akande, O.J. (2023), "Mechanical and microstructural properties of expanded polyethylene powder/mica filled hybrid polystyrene composites", *Mech. Adv. Mater. Struct.*, **30**, 2610-2619. https://doi.org/10.1080/15376494.2022.2062488
Afzali, M., Farrokh, M. and Carrera, E. (2022), "Thermal buckling loads of rectangular FG plates with temperature-dependent properties using Carrera Unified Formulation", *Compos. Struct.*, **295**, 115787. https://doi.org/10.1016/j.compstruct.2022.115787
Ahlawat, N. and Saini, R. (2024), "Vibration and buckling analysis of elastically supported bi-directional fgm mindlin circular plates having variable thickness", *J. Vib. Eng. Tech.*, **12**, 513-532. https://doi.org/10.1007/s42417-023-00856-1
Ai, L. and Gao, X.L. (2017), "Metamaterials with negative Poisson's ratio and non-positive thermal expansion", *Compos. Struct.*, **162**, 70-84. https://doi.org/10.1016/j.compstruct.2016.11.076
Akgöz, B. and Civalek, Ö. (2018), "Vibrational characteristics of embedded microbeams lying on a two-parameter elastic foundation in thermal environment", *Compos. Part B Eng.*, **150**, 68-77. https://doi.org/10.1016/j.compositesb.2018.05.023
Al-Furjan, M., Fan, S., Shan, L., Farrokhian, A., Shen, X. and Kolahchi, R. (2023), "Wave propagation analysis of micro air vehicle wings with honeycomb core covered by porous FGM and nanocomposite magnetostrictive layers", *Waves Random Complex Med.*, **33**, 1-30. https://doi.org/10.1080/17455030.2023.2219935
Alhazmi, H., Shah, S.A.R., Anwar, M.K., Raza, A., Ullah, M.K. and Iqbal, F. (2021), "Utilization of polymer concrete composites for a circular economy: A comparative review for assessment of recycling and waste utilization", *Polymers*, **13**, 2135. https://doi.org/10.3390/polym13132135
Al-Osta, M.A. (2022), "An exponential-trigonometric quasi-3D HSDT for wave propagation in an exponentially graded plate with microstructural defects", *Compos. Struct.*, **297**, 115984. https://doi.org/10.1016/j.compstruct.2022.115984
Barooti, M.M., Safarpour, H. and Ghadiri, M. (2017), "Critical speed and free vibration analysis of spinning 3D single-walled carbon nanotubes resting on elastic foundations", *Eur. Phys. J. Plus*, **132**, 1-21. https://doi.org/10.1140/epjp/i2017-11698-x
Bert, C.W. and Malik, M. (1996), "Differential quadrature method in computational mechanics: a review", *Appl. Mech. Rev.*, **49**, 1-28. https://doi.org/10.1115/1.3101882
Duc, L.B., Le, B.T., Quoc, K.D., Tran, T.B. and Singh, R. (2025), "Investigation the effects of compaction pressure and sintering temperature on mechanical properties of Al-x% TiC composite", *Adv. Mater. Res.*, **14**(1), 71-79. https://doi.org/10.12989/amr.2025.14.1.071
Ebrahimi, F., Nouraei, M. and Seyfi, A. (2022), "Wave dispersion characteristics of thermally excited

graphene oxide powder-reinforced nanocomposite plates", *Waves Random Complex Med*., **32**, 204-232. https://doi.org/10.1080/17455030.2022.2032868

Ebrahimi, F. and Mahinzare, M. (2025), "Nonlinear vibration analysis of sandwich plate with cellular auxetic core and porous GPL reinforced piezoelectric face sheets rested on elastic foundation using GDQM via Reddy plate theory", *Structures*, **77**, 108976. https://doi.org/10.1016/j.istruc.2024.108976

Fuyad, S.T.M., Al Bari, M.A., Makfidunnabi, M., Nain, H.Z., Özdemir, M.E. and Yaylacı, M. (2024), "Finite element analysis of ratcheting on beam under bending-bending loading conditions", *Struct. Eng. Mech.*, **89**(1), 23-31. https://doi.org/10.12989/sem.2024.89.1.023

Garg, A., Belarbi, M.O., Li, L., Chalak, H., Tounsi, A. and Zenkour, A. (2024), "Comparative study on the buckling analysis of exponential, power and sigmoidal sandwich FGM plates under hygro-thermal conditions", *Adv. Mater. Res.*, **13**(5), 431-462. https://doi.org/10.12989/amr.2024.13.5.431

Jayakumari, B.Y., Swaminathan, E.N. and Partheeban, P. (2024), "Sustainable construction material using nanosilica and multi-walled carbon nanotubes in cement concrete", *Adv. Nano Res.*, **16**(5), 459-472. https://doi.org/10.12989/anr.2024.16.5.459

Jha, D., Kant, T. and Singh, R.K. (2012), "Higher order shear and normal deformation theory for natural frequency of functionally graded rectangular plates", *Nuclear Eng. Des.*, **250**(5), 8-13. https://doi.org/10.1016/j.nucengdes.2012.05.001

Kaleni, A., Magagula, S.I., Motloung, M.T., Mochane, M.J. and Mokhena, T.C. (2022), "Preparation and characterization of coal fly ash reinforced polymer composites: An overview", *Express Polym. Lett.*, **16**, 68-91. https://doi.org/10.3144/expresspolymlett.2022.6

Lezgy-Nazargah, M., Yaylacı, M. and Shad, H. (2025), "Double superposition shear deformation theory for buckling analysis of layered composite circular closed cylindrical shells in underwater environments", *Ocean Eng.*, **340**, 122230. https://doi.org/10.1016/j.oceaneng.2024.122230

Nikmehr, B. and Al-Ameri, R. (2022), "A state-of-the-art review on the incorporation of recycled concrete aggregates in geopolymer concrete", *Recycling*, **7**, 51. https://doi.org/10.3390/recycling7050051

Rahimi, A., Alibeigloo, A. and Safarpour, M. (2020), "Three-dimensional static and free vibration analysis of graphene platelet-reinforced porous composite cylindrical shell", *J. Vib. Control*, **26**, 1627-1645. https://doi.org/10.1177/1077546320910780

Reddy, J.N. (2003), *Mechanics of laminated composite plates and shells: theory and analysis*, CRC press.

SafarPour, H., Hosseini, M. and Ghadiri, M. (2017), "Influence of three-parameter viscoelastic medium on vibration behavior of a cylindrical nonhomogeneous microshell in thermal environment: An exact solution", *J. Therm. Stress.*, **40**, 1353-1367. https://doi.org/10.1080/01495739.2017.1350826

Safarpour, M., Rahimi, A., Alibeigloo, A., Bisheh, H. and Forooghi, A. (2021a), "Parametric study of three-dimensional bending and frequency of FG-GPLRC porous circular and annular plates on different boundary conditions", *Mech. Based Des. Struct.*, **49**, 707-737. https://doi.org/10.1080/15397734.2020.1713156

Safarpour, M. and Alibeigloo, A. (2021b), "Elasticity solution for bending and frequency behavior of sandwich cylindrical shell with FG-CNTRC face-sheets and polymer core under initial stresses", *Int. J. Appl. Mech.*, **13**, 2150020. https://doi.org/10.1142/S1758825121500204

Safarpour, M., Safarpour, H. and Civalek, O. (2025), "Wave propagation analysis of functionally graded bio-composite circular plates using an improved sinusoidal shear deformation theory resting on an advanced viscoelastic foundation", *Eur. J. Mech. A Solids*, **112**, 105688. https://doi.org/10.1016/j.euromechsol.2025.105688

Sekban, D.M., Yaylacı, E.U., Özdemir, M.E., Öztürk, Ş., Yaylacı, M. and Panda, S.K. (2024a), "Formability behavior of AH-32 shipbuilding steel strengthened by friction stir process", *Theor. Appl. Fract. Mech.*, **132**, 104485. https://doi.org/10.1016/j.tafmec.2024.104485

Sekban, D.M., Yaylaci, E.U., Ozdemir, M.E. and Yaylaci, M. (2024b), "Determination of formability behavior of steel used in ships by various methods", *Struct. Eng. Mech.*, **92**(2), 189-196. https://doi.org/10.12989/sem.2024.92.2.189

Selvamani, R., Thangamuni, P., Yaylacı, M., Emin Özdemir, M. and Yaylacı, E.U. (2024a), "Nonlinear vibration and parametric excitation of magneto-thermo elastic embedded nanobeam using homotopy perturbation technique", *ZAMM J. Appl. Math. Mech.*, **104**, e202400525.

https://doi.org/10.1002/zamm.202400525
Selvamani, R., Ebrahimi, F., Yaylacı, M., Öztürk, Ş. and Yaylacı, E.U. (2024b), "Nonlinear poro-thermo-forced vibration in curved sandwich magneto-electro-elastic shells under hygrothermal environment", *Acta Mechanica*, **235**, 5489-5528. https://doi.org/10.1007/s00707-024-04036-4
Selvamani, R., Prabhakaran, T., Yaylacı, M., Kartal, Ş.E. and Yaylacı, E.U. (2025), "Doublet structural modeling of nonhomogeneous Euler mass sensor nanobeams using boundary characteristics Bernstein Polynomials", *ZAMM J. Appl. Math. Mech.*, **105**, e202401264. https://doi.org/10.1002/zamm.202401264
Song, M., Kitipornchai, S. and Yang, J. (2017), "Free and forced vibrations of functionally graded polymer composite plates reinforced with graphene nanoplatelets", *Compos. Struct.*, **159**, 579-588. https://doi.org/10.1016/j.compstruct.2016.09.070
Zouatnia, N. and Hadji, L. (2019), "Static and free vibration behavior of functionally graded sandwich plates using a simple higher order shear deformation theory", *Adv. Mater. Res.*, **8**(4), 313-335. https://doi.org/10.12989/amr.2019.8.4.313

CC